

Cost-efficient anthropomorphic head phantom for quantitative image quality assessment in cone beam CT

Wang, Yichao; Dankelman, Jenny; Ruijters, Danny

DOI

[10.1088/2057-1976/aca02d](https://doi.org/10.1088/2057-1976/aca02d)

Publication date

2022

Document Version

Final published version

Published in

Biomedical Physics and Engineering Express

Citation (APA)

Wang, Y., Dankelman, J., & Ruijters, D. (2022). Cost-efficient anthropomorphic head phantom for quantitative image quality assessment in cone beam CT. *Biomedical Physics and Engineering Express*, 8(6), Article 065038. <https://doi.org/10.1088/2057-1976/aca02d>

Important note

To cite this publication, please use the final published version (if applicable). Please check the document version above.

Copyright

Other than for strictly personal use, it is not permitted to download, forward or distribute the text or part of it, without the consent of the author(s) and/or copyright holder(s), unless the work is under an open content license such as Creative Commons.

Takedown policy

Please contact us and provide details if you believe this document breaches copyrights. We will remove access to the work immediately and investigate your claim.

Green Open Access added to TU Delft Institutional Repository

'You share, we take care!' - Taverne project

<https://www.openaccess.nl/en/you-share-we-take-care>

Otherwise as indicated in the copyright section: the publisher is the copyright holder of this work and the author uses the Dutch legislation to make this work public.

PAPER

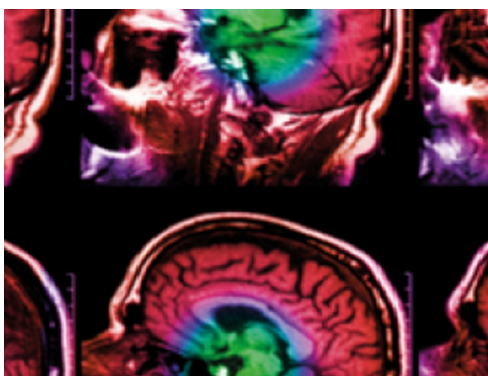
Cost-efficient anthropomorphic head phantom for quantitative image quality assessment in cone beam CT

To cite this article: Yichao Wang *et al* 2022 *Biomed. Phys. Eng. Express* **8** 065038

View the [article online](#) for updates and enhancements.

You may also like

- [Autoregressive Planet Search: Application to the Kepler Mission](#)
Gabriel A. Caceres, Eric D. Feigelson, G. Jogesh Babu *et al.*
- [Feasibility of wireless cardiorespiratory monitoring with dry electrodes incorporated in a belt in preterm infants](#)
Anouk W J Scholten, Ruud W van Leuteren, Cornelia G de Waal *et al.*
- [A momentum-based diffeomorphic demons framework for deformable MR-CT image registration](#)
R Han, T De Silva, M Ketcha *et al.*



IPEM | IOP

Series in Physics and Engineering in Medicine and Biology

Your publishing choice in medical physics,
biomedical engineering and related subjects.

Start exploring the collection—download the
first chapter of every title for free.

Biomedical Physics & Engineering Express



PAPER

Cost-efficient anthropomorphic head phantom for quantitative image quality assessment in cone beam CT

RECEIVED
9 September 2022

REVISED
26 October 2022

ACCEPTED FOR PUBLICATION
4 November 2022

PUBLISHED
15 November 2022

Yichao Wang^{1,*} , Jenny Dankelman² and Danny Ruijters¹ 

¹ Philips Healthcare, Dept. of Image Guided Therapy, The Netherlands

² Delft University of Technology, Department of Biomechanical Engineering, The Netherlands

* Author to whom any correspondence should be addressed.

E-mail: liang.wang@philips.com, j.dankelman@tudelft.nl and danny.ruijters@philips.com

Keywords: anthropomorphic head phantom, cone beam computed tomography, image quality assessment, radiodensity, scatter, tissue equivalent materials

Abstract

In this study, a novel anthropomorphic head phantom for quantitative image quality assessment in cone beam computed tomography (CBCT) is proposed. The phantom is composed of tissue equivalent materials (TEMs) which are suitable for cost-efficient fabrication methods such as silicone casting and 3D printing. A monocalcium phosphate/gypsum mixture (MCPHG), nylon and a silyl modified polymer gel (SMP) are proposed as bone, muscle and brain equivalent materials respectively. The TEMs were evaluated for their radiodensity in terms of Hounsfield Units (HU) and their x-ray scatter characteristics. The median radiodensity and inter quartile range (IQR) of the MCPHG and SMP were found to be within the range of the theoretical radiodensity for bone and brain tissue: 922 (IQR = 156) and 47 (IQR = 7) HU respectively. The median radiodensity of nylon was slightly outside of the HU range of muscle tissue, but within the HU range of a combination of muscle and adipose tissue: -18 (IQR = 40) HU. The median ratios between the measured scatter characteristics and simulated tissues were between 0.84 and 1.13 (IQR between 0.05 and 0.14). The preliminary results of this study show that the proposed design and TEMs are potentially suitable for the fabrication of a cost-efficient anthropomorphic head phantom for quantitative image quality assessment in CT or CBCT.

1. Introduction

Cone beam computed tomography (CBCT) is a state of the art technique for medical imaging using x-rays, with a broad range of applications. For example, CBCT C-arm systems, such as the Philips Allura FD20 (Philips Healthcare, Best, the Netherlands), can be used for diagnostic and peri-interventional imaging (e.g. to make an angiography or a 3D reconstruction of the anatomy). While CBCT systems can produce images with excellent spatial resolution, the contrast resolution is still somewhat inferior in comparison with other imaging techniques, such as traditional (fan beam) CT and magnetic resonance imaging (MRI) [1, 2]. The low contrast resolution results in a less distinctive visualization of the brain tissue, which can limit the diagnostic applications of CBCT systems. The contrast resolution of the images created with CBCT systems suffers among others from the effects of

scatter radiation. Researchers have investigated several promising methods to enhance the contrast resolution, by implementing fast and accurate correction techniques for scatter radiation. The enhanced image quality is often physically assessed using phantoms, for example by Maher, Gao and Baer [3–5] (among others). The phantoms that were used can generally be categorized as simple geometry phantoms or as anthropomorphic phantoms. Simple geometry phantoms such as the Catphan 600 (the phantom laboratory, Salem, New York, USA) are often equipped with low contrast and spatial resolution inserts for quantitative image quality assessment (IQA), but the scatter characteristics of such phantoms are not representative due to the simplified shape. Anthropomorphic phantoms represent anatomical features of the human head and are constructed using tissue equivalent materials (TEMs). These phantoms are therefore more likely to have realistic attenuation characteristics.

Unfortunately, a limited range of commercial anthropomorphic head phantoms is available and these phantoms have certain limitations. For example, the commonly used Rando Alderson (Radiology Support Devices, Carson, California, USA) phantom is composed of TEMs that show an underattenuation (in terms of Hounsfield Units) in the lower diagnostic energy range of the x-ray photons [6], which can result in a biased interpretation of the (enhanced) image quality. Also, along with other anthropomorphic phantoms, such as the ACS (Kyoto Kagaku, Kyoto, Japan) and the Atom Max (Computerized Imaging Reference systems inc, Norfolk, Virginia, USA), these phantoms lack inserts for the measurement of the contrast and spatial resolution of the image. Some researchers have ordered modified commercial phantoms [7] or even constructed new phantoms, by adding inserts for low contrast resolution [8], but modified phantoms are relatively expensive and limit the accessibility for wide usage. Furthermore, while scatter radiation is an important factor in the interaction between the x-ray photons and the matter these photons pass through, the scatter characteristics of the TEMs are hardly investigated. Geraldelli [9] has investigated the scatter characteristics of several TEMs including adipose, muscle and bone equivalent materials and Kozanetzky [10] has investigated the scatter characteristics of some plastic materials, but these studies only reported on the coherent scattering characteristics for a specific scattering angle, while incoherent scatter also contributes in the interaction between the x-ray photons and matter in the lower diagnostic energy range and it is of interest to know the spatial distribution of scatter radiation for IQA purposes. It is therefore of interest to address the shortcomings of the previously mentioned issues, by developing an anthropomorphic phantom which is (1) suitable for quantitative image quality assessment, (2) has materials with representative attenuation (both radiodensity and scatter) characteristics and (3) is suitable for cost-efficient fabrication techniques for a wider accessibility.

Next to documenting a realistic anthropomorphic phantom that can be manufactured using readily available and cost efficient techniques, we particularly paid attention to characterizing the suitability of the chosen materials in terms of their equivalence to human tissues, not only regarding their radiodensity, but also with respect to their x-ray scattering properties. Especially, the scatter aspects are often overlooked, while they play an important role in the image quality achieved by cone-beam CT acquisitions.

2. Method

2.1. CBCT-data based design of the phantom

The design of the phantom was based on a 3D model of the human head, obtained from anonymous CBCT

data of a male, similar to the methodology used by Kim [11]. The data (DICOM format) for this study were obtained from a head XperCT protocol (Allura FD20, Philips Healthcare, Best, the Netherlands) and manually segmented into a skull mesh and into a soft tissue outer shell mesh (STL format) (figure 1) by adjusting the threshold of the intensity of the CBCT image. The STL meshes (available upon request by sending an e-mail to the corresponding author.) were post-processed using an open source mesh editing program (Blender, Amsterdam, the Netherlands), by manually closing holes in the maxillofacial region of the skull and by increasing the thickness of this region in order to increase the mechanical strength of the area. The skull was divided into three horizontally cut sections (the calvaria, maxilla and mandible) (figures 1(a) and (b)). Cylindrical (low) contrast inserts were positioned at the posterior area of the cranial cavity and a model of the ventricles, containing cerebrospinal fluid, was manually positioned within the cranial cavity (figures 1(a) to (c)). The 'muscle tissue' shell was divided into two vertically cut sections (figure 1(d)). There was no design of the brain needed since the brain equivalent material of the phantom is a polymer-based gel (see section 2.2).

2.2. Tissue equivalent materials

In previous studies, several researchers have investigated materials for the suitability as TEM for radiological purposes, including for dosimetry and for the construction of phantoms. These materials were often compared with human tissues in terms of mass attenuation coefficient (μ_m). Recommended bone equivalent materials include 'B-100' bone equivalent plastic and poly-vinylchloride [12], a dolomite-PMMA resin mixture [13], a dipotassium phosphate based mixture [14] and a custom epoxy-resin based mixture [15]. Recommended muscle equivalent materials include nylon [16], water [9, 17] and custom epoxy resin based mixtures, including 'Rando Alderson soft tissue equivalents' [8] and an Araldite-based mixture [15] (for a pediatric phantom).

Because the majority of the recommended TEMs were evaluated for usage in dosimetry and because not all of these materials were suitable for the specified fabrication techniques (e.g. silicone casting and 3D printing), only nylon was considered as potential muscle equivalent material and selected for further evaluation in this study. Two novel TEMs for bone tissue and brain tissue are also proposed in this study, which are a mixture of monocalcium phosphate (MCPH) ($Ca(H_2PO_4)_2$), calcium sulfate ($CaSO_4$) and water (referred to as 'MCPHG') as bone equivalent material (3.85 wt% MCPH, 60 wt% $CaSO_4$ and 36.15 wt% water respectively) and a commercially available silyl-modified polymer gel (SMP) (Bison Polymax Crystal, Bolton adhesives, Rotterdam, the Netherlands) as brain equivalent material. The mass attenuation coefficient (μ_m) of the TEMs were obtained from the

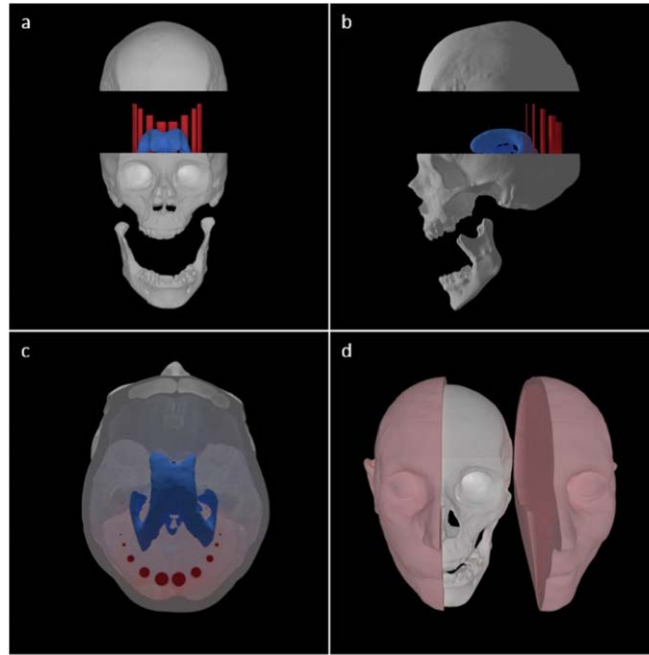


Figure 1. CBCT data based design (a) anterior-posterior view of the skull mesh, containing inserts (red) and ventricles containing cerebrospinal fluid (blue). (b) left lateral view of the skull mesh (c) axial superior-inferior view of the skull mesh (no calvaria) with the low contrast inserts at the posterior side of the skull (red) and the ventricles (blue). (d) vertically cut muscle shell mesh, surrounding the skull mesh.

Table 1. Mass attenuation coefficient (μ_m) at 60, 80, 100 and 150 keV and physical density (ρ) of proposed tissue equivalent materials (TEMs) [18, 19].

Tissue/TEM	$\mu_m(60 \text{ keV})$	$\mu_m(80 \text{ keV})$	$\mu_m(100 \text{ keV})$	$\mu_m(150 \text{ keV})$	$\rho [\text{g cm}^{-3}]$
Bone	0.315	0.222	0.186	0.148	1.92
Muscle	0.205	0.182	0.169	0.149	1.05
Brain	0.206	0.183	0.17	0.15	1.05
CSF/water	0.206	0.184	0.171	0.151	1.00
MCPHG	0.314	0.223	0.187	0.149	2.3
Nylon (PA12)	0.195	0.179	0.169	0.150	1.01
SMP	0.248	0.196	0.173	0.145	1.05

online photon cross section database XCOM [18]), provided by the National Institute of Standards and Technology (NIST). The μ_m of the tissues and the physical density (ρ) were obtained from the International Commission on Radiation Units and Measurements (ICRU) report 44 [19] and presented in table 1.

2.3. Radiodensity

The theoretical radiodensity of the TEMs were calculated using the linear attenuation coefficient (μ_x), by multiplying the mass attenuation coefficient of the TEMs with the physical density (ρ) of the TEM from table 1 (equation (1)). Then the radiodensity in [HU] was then calculated using equation (2).

$$\mu_x = \mu_m \rho. \quad (1)$$

Where μ_x is the linear attenuation coefficient of the TEM and ρ is the physical density of the TEM.

$$HU = 1000 \frac{\mu_x - \mu_{water}}{\mu_{water}} \quad (2)$$

Where μ_x and μ_{water} are the linear attenuation coefficient of the TEM and water respectively.

A Philips Allura FD20 x-ray system (Philips Healthcare, Best, the Netherlands) was used to measure the radiodensity of the TEM samples. The TEM samples were placed at the head side of the patient table (Maquet holding B.V. & Co. KG, Rastatt, Germany) along with a calibration phantom with known HU values (QRM-2DMC, QRM, Moehrendorf, Germany). A Head XperCT low dose, fast acquisition protocol was performed (at 120 kVp) for the acquisition of the 3D reconstructed image of each TEM.

The median HU value and inter quartile range (IQR) of each TEM were calculated after manually assessing the HU value at 10 points at three different slices (so 30 in total) of the 3D volume.

The calibration phantom was used to check for a bias in the measured HU values of the TEM samples

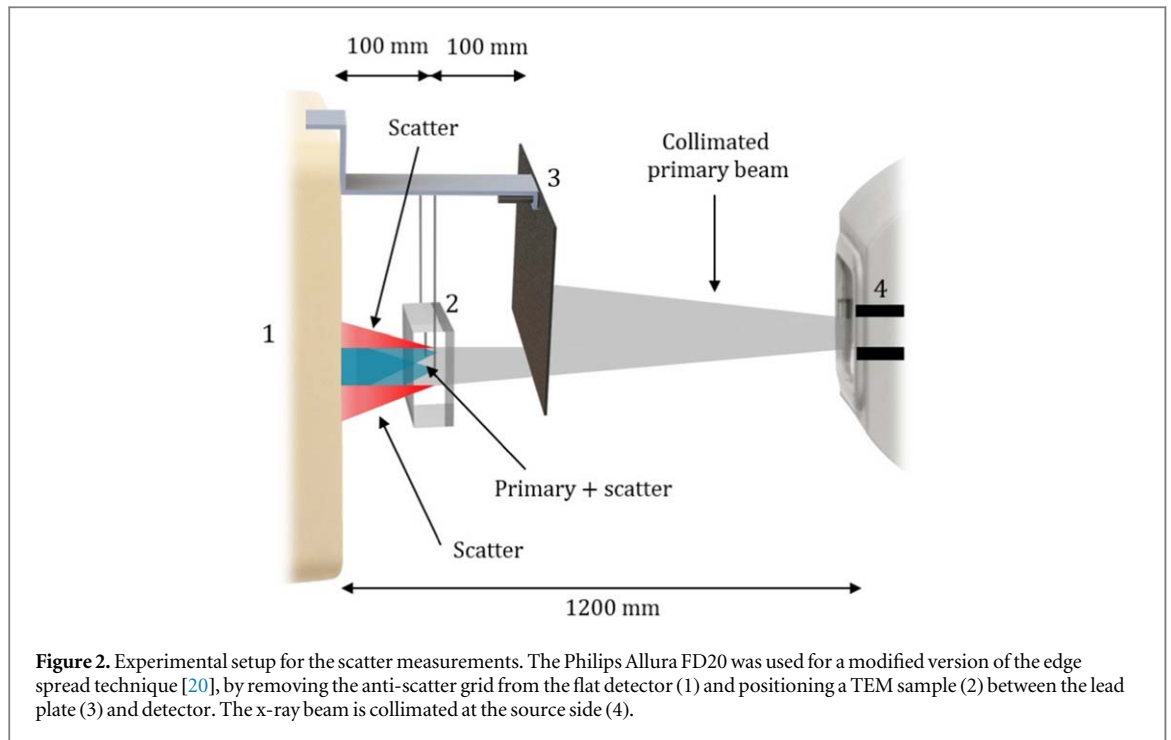


Figure 2. Experimental setup for the scatter measurements. The Philips Allura FD20 was used for a modified version of the edge spread technique [20], by removing the anti-scatter grid from the flat detector (1) and positioning a TEM sample (2) between the lead plate (3) and detector. The x-ray beam is collimated at the source side (4).

and to check for scaling effects and non-linearities of the HU scale. The results of the (calibration) measurements are presented in section 3.2 of the results.

2.4. Scatter characteristics

The same Allura FD20 x-ray system as the one for the radiodensity measurements was used to measure the scatter characteristics of the proposed TEMs. A modified version of the edge spread technique for scatter quantification [20] was used, by positioning a lead plate 200 mm in front of the flat detector of the Allura (after removal of the anti-scatter grid) in order to block the top side of the incident x-ray beam. The three remaining sides were blocked using built in collimators at the source side of the x-ray system, so only the TEM would be radiated. TEM samples of 20 mm, 40 mm and 60 mm thickness (100×100 mm width and height) were positioned behind the lead plate, 100 mm from the detector and 15 fluoroscopic images (in order to reduce the image noise) were taken at 60, 80, 100 and 120 kVp (at 100 mA) per TEM sample. The x-ray source to detector distance was 1200 mm. The photons of the incident x-ray beam that pass through the TEM sample are partially scattered and these scattered photons fall on the region of the flat detector behind the lead plate (figure 2).

Analysis of the intensity along a vertical pixel line at the center of the detector (in portrait mode) results in a characteristic intensity function, called the edge spread function (ESF), which is a function of the pixel position (x) on the detector (figure 3). The scatter characteristics of the TEMs, obtained by processing of the mean ESF (from the 15 fluoroscopic images), were defined in terms of scatter magnitude and spatial scatter distribution. The scatter magnitude was further

defined as the maximal scatter to primary ratio (MSPR) of the TEM (equation (3)) and the scatter magnitude at the edge of the lead plate (EM) (equation (4)). The spatial scatter distribution (SD) was quantified as the pixel position behind the lead plate where the normalized scatter intensity reached 0.02 (figure 3). The value of 0.02 was selected because this point of the scatter function was most distinctive for each TEM with different thickness.

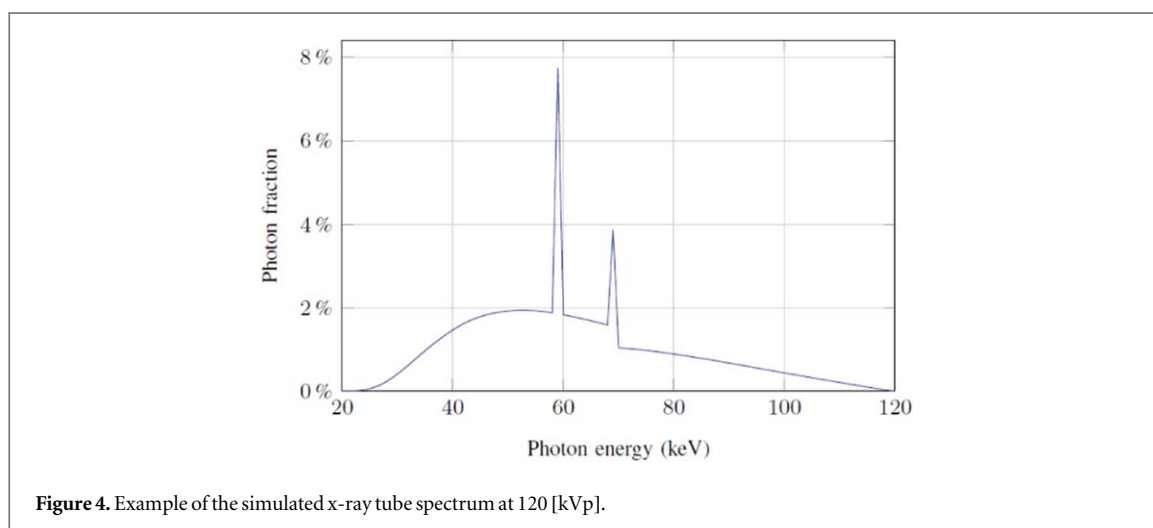
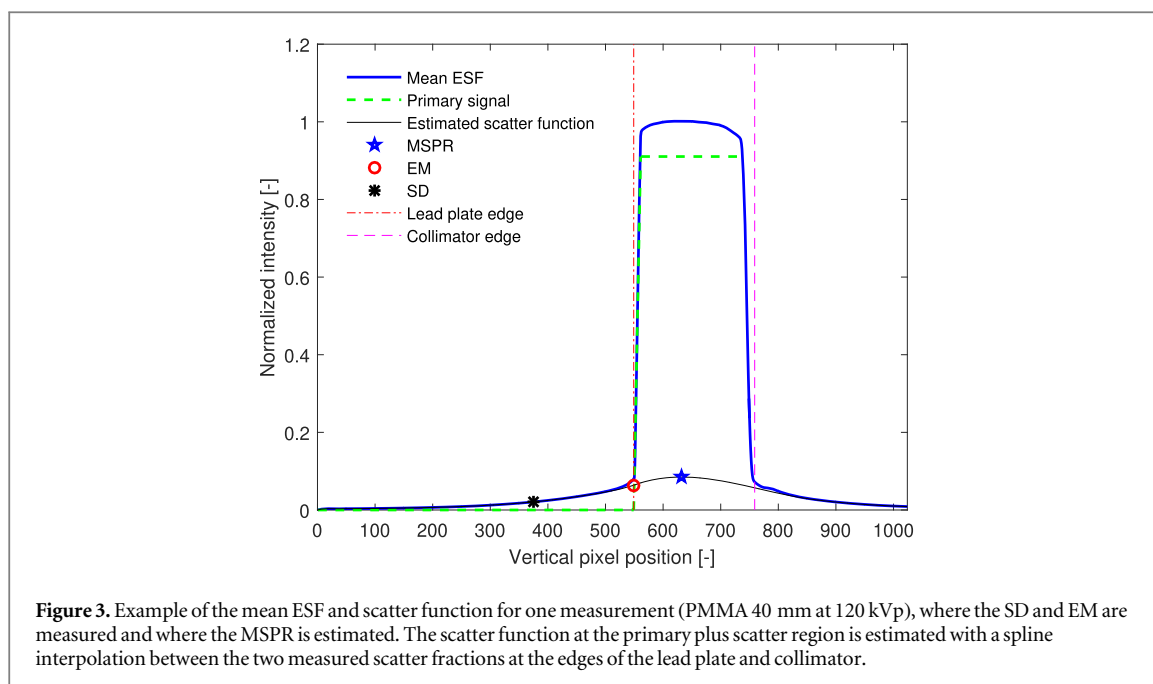
$$MSPR = \frac{\max(S(x))}{P(x)} \quad (3)$$

Where $S(x)$ is the scatter function as a function of the pixel position (x) on the detector, obtained from the ESF(x) and $P(x)$ is the primary function after subtracting $S(x)$ from the ESF(x).

$$EM = \max\left(\frac{d^2ESF(x)}{dx^2}\right) \quad (4)$$

The setup was calibrated to correct for the heel effect and for veiling glare of the detector. The heel effect, caused by the anode of the x-ray system, results in a gradient in the ESF and the effects of veiling glare on a flat detector can result in an overestimation of the scatter signal of up to 15% [21]. The scatter function was estimated by applying a spline interpolation between the two scatter fractions behind the lead plate and the collimator, using the angles of the scatter fractions at the edge.

The experimental setup and data processing methodology were validated by comparing the physical measurements of polymethylmethacrylate (PMMA) samples with Monte Carlo (MC) scatter simulations (based on [22, 23]) of PMMA samples with the same thicknesses at the same tube voltages (see figure 4 for



an example of the simulated x-ray tube spectrum at 120 kVp).

2.5. Prototype fabrication

A prototype of the right anterior part of the designed phantom (figure 5(a)) was fabricated using the proposed TEMs (this part of the head was selected because it contains all relevant TEMs and several inserts). Cost-efficient methods were used to fabricate the prototype. The MCPHG skull was fabricated using silicone casting (shore 15 silicone casting rubber, Polyester-shoppen B.V., Moordrecht, the Netherlands), where a positive mold of the skull (two pieces) was fabricated using FDM printing (Ultimaker 2, Geldermalsen, the Netherlands) (figures 5(b) and (c)). The initially liquid MCPHG (see section 2.2 for composition) was stirred with intervals for approximately one hour in order to remove air bubbles that emerged during the hardening of the mixture, before being poured into the cast. The

SMP-gel was injected into the cranial cavity of the skull using a silicone kit injector and the muscle shell was fabricated using selective laser sintering of nylon powder (modified polyamide 12 powder) (Shapeways, Eindhoven, the Netherlands) (figure 5(d)). After the prototype was assembled it was held in place by fixing PMMA plates to the flat surfaces until everything was solidified.

3. Results

3.1. Comparison of measurements with and simulations

The MSPR, EM and SD ratios between the measurements and MC simulations for measurements at two different test labs were 0.87, 1.00, 1.00 and 1.03, 1.13, 0.96 (IQRs between 0.05 and 0.14) (figure 6) and therefore the experimental setup and estimation methodology were considered valid.

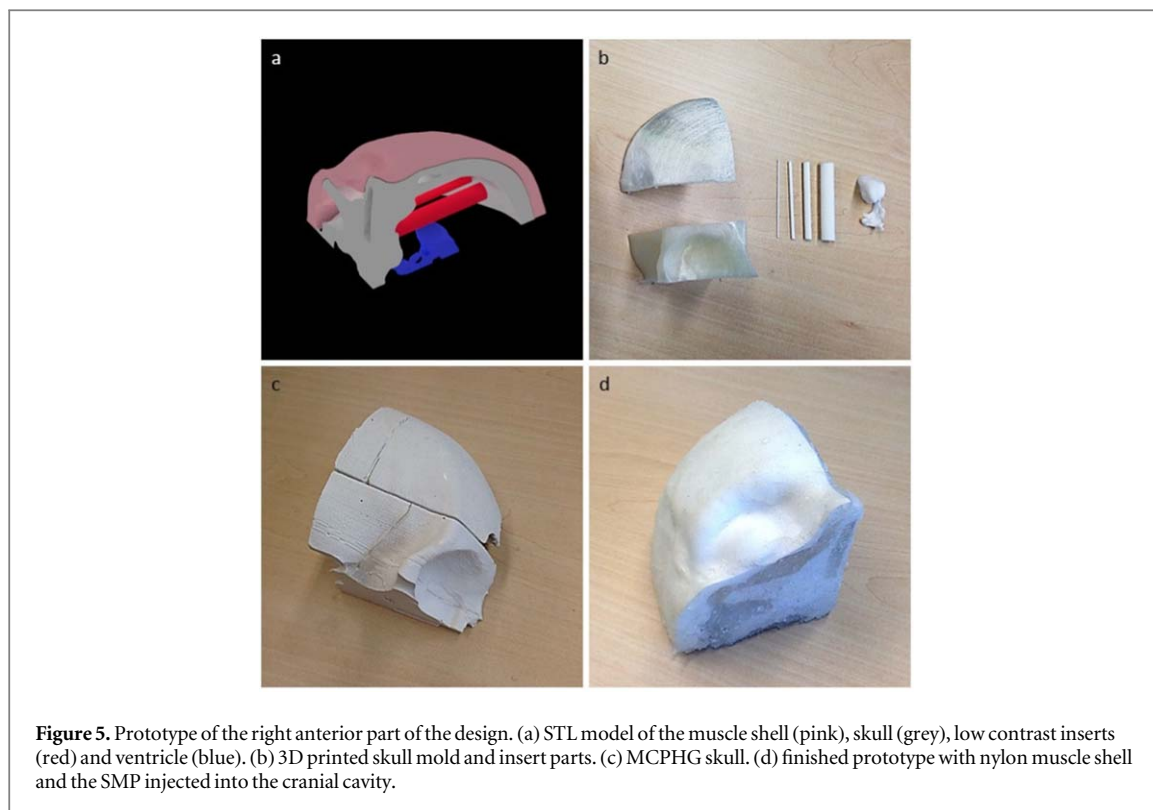


Figure 5. Prototype of the right anterior part of the design. (a) STL model of the muscle shell (pink), skull (grey), low contrast inserts (red) and ventricle (blue). (b) 3D printed skull mold and insert parts. (c) MCPHG skull. (d) finished prototype with nylon muscle shell and the SMP injected into the cranial cavity.

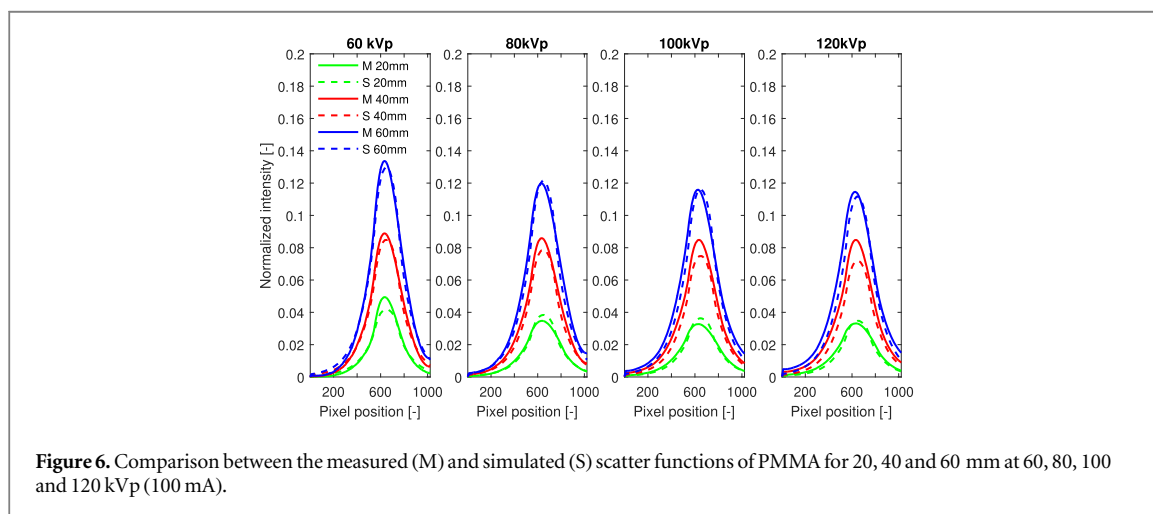


Figure 6. Comparison between the measured (M) and simulated (S) scatter functions of PMMA for 20, 40 and 60 mm at 60, 80, 100 and 120 kVp (100 mA).

Table 2. The median, 25th percentile (Q1), 75th percentile (Q3) of the measured HU values for the calibration phantom (CP), and TEMs are summarized along with the calculated HU values using equation (2) of the CP and TEMs and along the theoretical HU range of tissues [24].

Material	Median (n = 30)	Q1	Q3	Theoretical HU value	Tissue HU range
CP 38	36	30	41	38	—
CP 13	11	4	17	13	—
CP -62	-54	-57	-50	-62	—
MCPHG	922	845	1001	1398	700-3000 (bone)
Nylon	-18	-41	-1	1	5-40 (muscle)
SMP	47	45	52	27	20-45 (brain)

3.2. Radiodensity of the TEMs

The calculated and measured HU values of MCPHG, nylon and SMP after calibration are visualized in figure 7 and summarized in table 2.

3.3. Scatter characteristics of the TEMs

The measured MSPR, EM and SD of MCPHG, nylon and SMP are plotted along MC simulations of bone, muscle and brain tissues in figure 8–10 respectively.

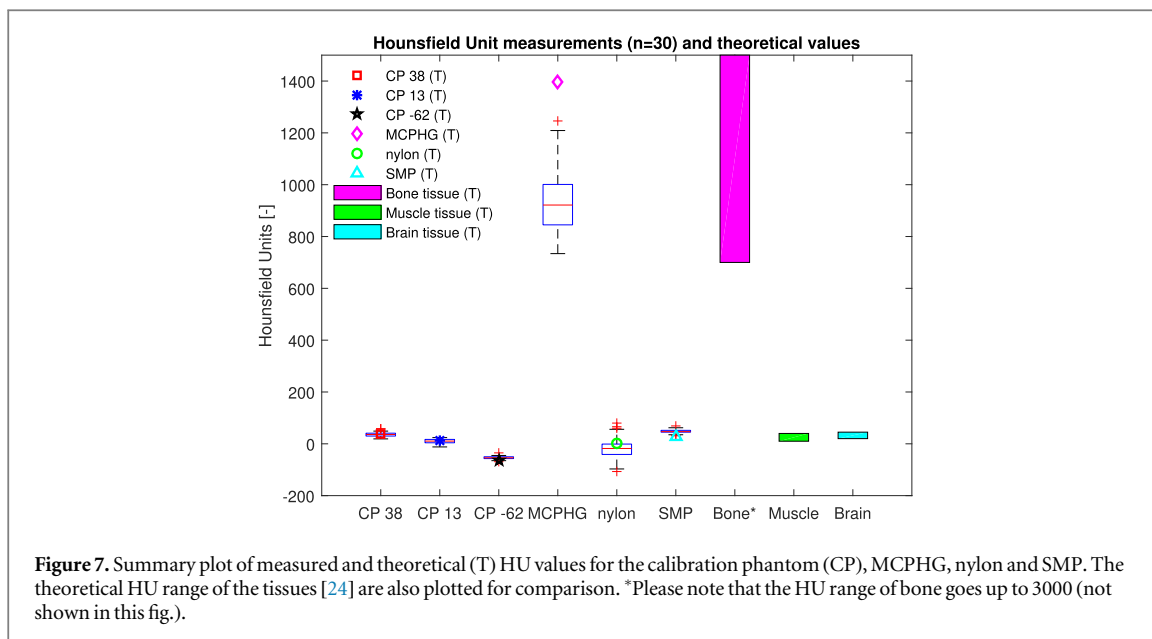


Figure 7. Summary plot of measured and theoretical (T) HU values for the calibration phantom (CP), MCPHG, nylon and SMP. The theoretical HU range of the tissues [24] are also plotted for comparison. *Please note that the HU range of bone goes up to 3000 (not shown in this fig.).

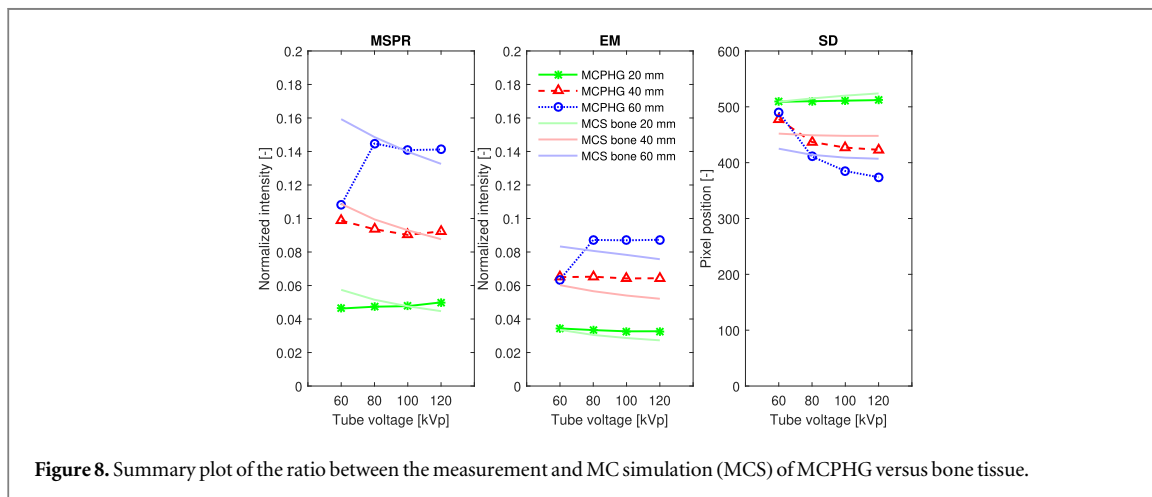


Figure 8. Summary plot of the ratio between the measurement and MC simulation (MCS) of MCPHG versus bone tissue.

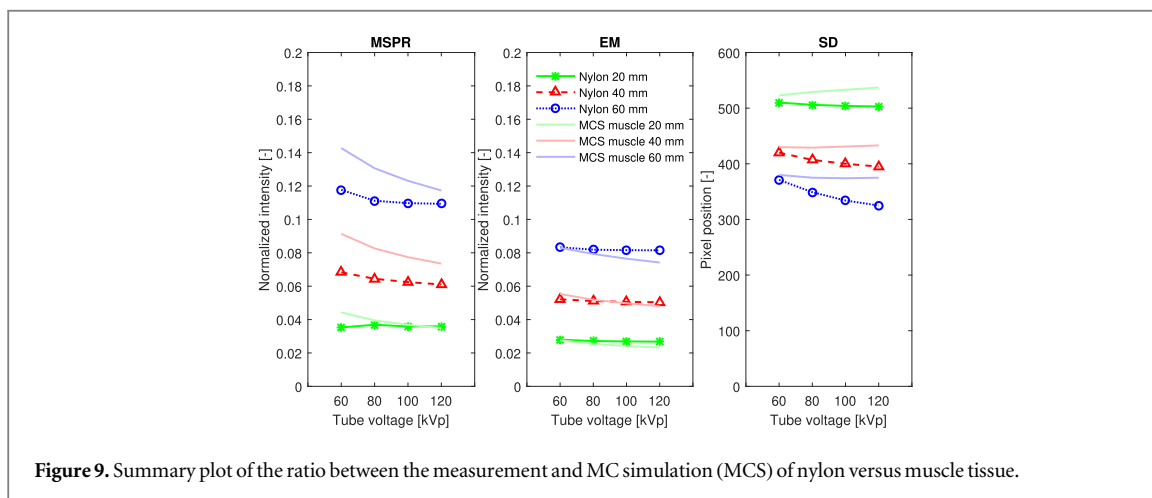


Figure 9. Summary plot of the ratio between the measurement and MC simulation (MCS) of nylon versus muscle tissue.

From these figures it can be seen that the overall scatter characteristics of the proposed TEMs are in good agreement with the simulated tissues, except for the MSPR, EM and SD of the 60 mm MCPHG

sample at 60 kVp, which are obviously lower in comparison with the MC simulation of bone tissue. After analysis of the estimated scatter function for this measurement, an inaccurate estimation of the scatter

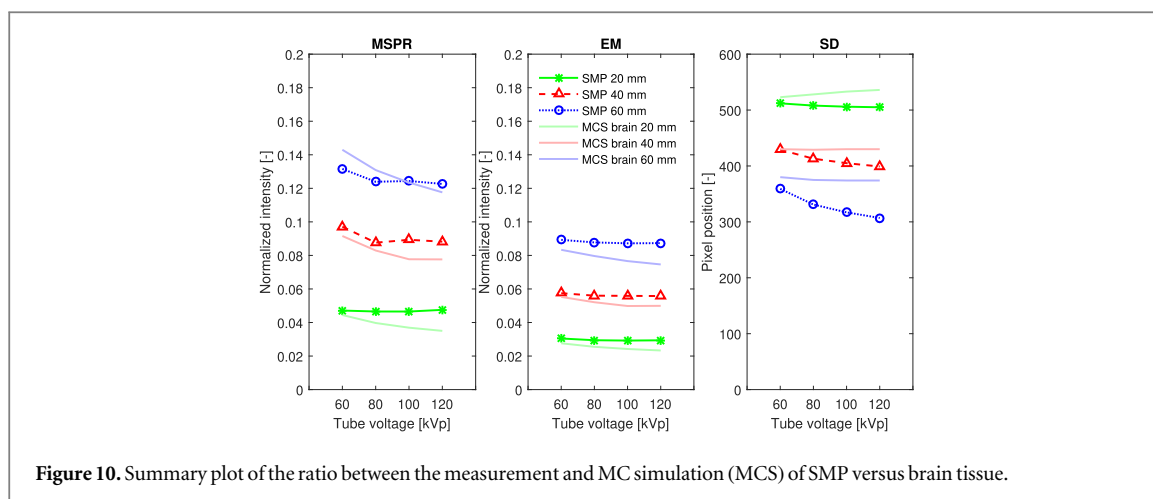


Figure 10. Summary plot of the ratio between the measurement and MC simulation (MCS) of SMP versus brain tissue.

Table 3. Summary of the median (Mdn) ratios and inter quartile range (IQR) between the measured TEMs and simulated tissues.

Material/ tissue	MSPR ratio		EM ratio		SD ratio	
	(n = 12)		(n = 12)		(n = 12)	
	Mdn	IQR	Mdn	IQR	Mdn	IQR
MCPHG/bone	0.95	0.13	1.13	0.10	0.98	0.05
Nylon/muscle	0.84	0.13	1.04	0.07	0.94	0.05
SMP/brain	1.06	0.14	1.12	0.07	0.94	0.06

function was observed due to a large presence of noise signals on the detector. It was therefore considered acceptable to exclude this measurement from the overall results. A summary of the MSPR, EM and SD ratios between the measured TEMs and simulated tissues are can be found in table 3.

3.4. Practical evaluation of the fabricated prototype

The practical aspects of the TEMs for actual usage for the construction of the phantom and imaging aspects (e.g. anatomical structures or image artifacts) of the prototype were compared with the anonymous CBCT data of the head. Feedback from experts in x-ray and CT image quality was used in order to verify the usability of the phantom.

From a qualitative comparison between the CBCT patient data and the constructed prototype (figure 11), several observations could be made. A difference was observed between the the structure of the skull from the patient data and the MCPHG skull. Real bone tissue in the skull is composed of cortical bone at the outer layers and trabecular bone between these layers and is therefore more radiodense at the outer layers in comparison with the center. The MCPHG skull showed a more homogeneous representation of the skull, although some minor differences in radiodensity were observed between the surface and the center of the MCPHG skull (figure 11(d)), where the surface appeared to be more radiodense in comparison with the center. Another observation that was

made was the presence of some relatively big air pockets within different areas of the prototype, especially at the region of the SMP, which represents the brain tissue (figure 11(f)). The inserts for the measurement of the contrast resolution and ventricles were visible and useful on all relevant patient views of the images (i.e. anterior-posterior, lateral and axial view).

4. Discussion

In this study, a head phantom was designed for quantitative IQA in CBCT. This design was made in order to solve several issues of existing commercial head phantoms for IQA in CBCT, including an under-attenuation of the materials in the lower diagnostic energy range, the lack of inserts for quantitative IQA and the relatively high costs of most of the phantoms. The current design is equipped with inserts for quantitative measurement of the contrast resolution and composed of TEMs that are suitable for simple fabrication techniques. The TEMs were quantitatively evaluated in terms of radiodensity, scatter characteristics and qualitatively evaluated in terms of the suitability for simple fabrication techniques and the presence of image artifacts.

The radiodensity of MCPHG and SMP were considered representative as bone and brain tissue respectively, since the measured median HU values were within the theoretical range HU values of bone and brain tissue. The median HU values of nylon were out of the range of the HU values for muscle tissue, but in the design of the outer muscle shell of the prototype, no adipose tissue was included. If adipose tissue were to be included into the muscle shell, the average HU value would be lower, because the theoretical HU value of adipose tissue varies between -100 and -50 [24]. Since adipose tissue is present in the outer layers of the human head, it is reasonable to consider nylon as a representative ‘soft tissue’ equivalent material, to be used in the outer shell of the phantom. However, the scatter characteristics of adipose tissue were not

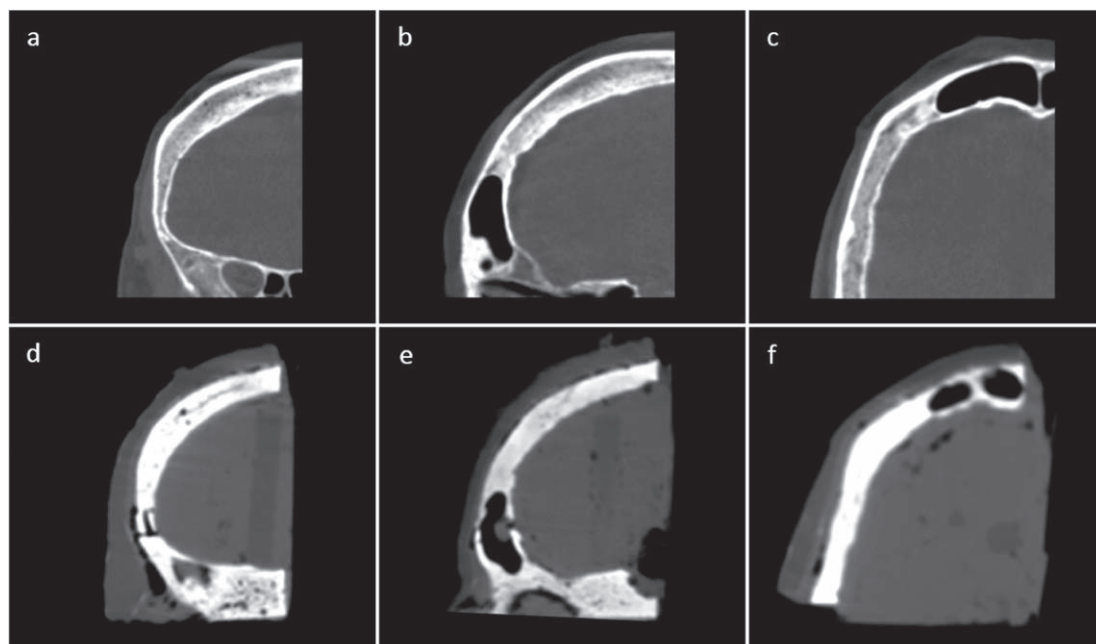


Figure 11. Comparison between the CBCT data of the anonymous patient head (a to c) and the prototype of the phantom with inserts for quantitative measurement of the contrast resolution (d to f). a and d: anterior-posterior view. b and e: left lateral view c and f: axial inferior-superior view. The inserts are visible in all relevant views and can be used for quantitative evaluation of the contrast resolution of the image.

taken into account in this study and should be included in the comparison in future work.

The median MSPR, EM and SD ratios between the measured TEMs and simulated tissues ranged from 0.84 to 1.13 and the IQR ranged from 0.05 to 0.14. By looking at the absolute difference in the normalized MSPR and EM signal, this means that the largest difference between the TEMs and simulated tissues was less than 3 percent. It is therefore reasonable to say that the proposed TEMs are representative as bone, muscle and brain equivalent materials, in terms of scatter characteristics.

The method for the quantification of the scatter characteristics was verified by comparing measurements of PMMA with Monte Carlo based scatter simulations of PMMA. While the verification was performed for multiple thicknesses at multiple tube voltages, the sample size was still considered too small for performing a sensitivity analysis about the accuracy and reliability of the measurements. It is recommended to perform the verification with a more diverse selections of materials in order to be able to draw conclusions about the accuracy and reliability of the measurements using this method.

While the scatter characteristics of the proposed TEMs were considered as representative for tissues in the head, more materials can be investigated using this technique, for example to find materials that have even better matching attenuation characteristics or are easier to work with. It is suggested to investigate the attenuation characteristics of calcium rich powders that are suitable for 3D printing, including mono-calcium phosphate powder, which was used in this

study, since researchers in the field of regenerative medicine have already shown that these calcium rich powders can be used to create durable and accurate scaffolds using 3D printing techniques, so this technique could be applied for the fabrication of the skull.

Based on the qualitative evaluation of the prototype, some improvements could be made. Especially the injection of the SMP into the cranial cavity should be carefully done, in order to minimize the amount of trapped air. Preliminary tests for injection using a wider nozzle show that it is possible to inject the SMP with virtually no air pockets. Furthermore, re-evaluation of the prototype after a time span of one month yielded that the initially homogeneously filled SMP showed shrinkage, resulting in similar (but larger) air pockets as from figure 11(f) in the brain area. A possible explanation of this phenomenon could be an effect of the drying process of the SMP. Therefore an alternative brain equivalent material could be considered.

Because the results of this current study are based on a partial prototype, a complete phantom should be fabricated and tested in order to demonstrate that the approach from this study can be applied in practice. Furthermore, a small series of phantoms should be fabricated and compared with each other in order to evaluate the consistency of the proposed materials and the reproducibility of the fabrication method.

5. Conclusions

The goal of this study was to investigate the feasibility of fabricating an anthropomorphic head phantom for


quantitative image quality assessment in CT and/or CBCT, with representative attenuation characteristics and inserts for the measurement of the contrast resolution. A prototype was fabricated using newly introduced TEMs which are suitable for fabrication techniques such as silicone casting and 3D printing. The measured radiodensity of the TEMs were in agreement with the radiodensity of the tissues that these TEMs should resemble and the scatter characteristics of the TEMs were evaluated and found to be representative as well. The design is suitable for simple fabrication techniques such as silicone rubber casting and 3D printing, which makes this phantom a potential alternative for researchers who want to fabricate (or customize) their own phantom at low costs.

Data availability statement

The data that support the findings of this study are available upon reasonable request from the authors.

ORCID iDs

Yichao Wang  <https://orcid.org/0000-0003-1309-3130>

Danny Ruijters  <https://orcid.org/0000-0002-9931-4047>

References

- [1] Söderman M *et al* 2008 Brain imaging with a flat detector C-arm: Technique and clinical interest of XperCT *Neuroradiology* **50** 863–8
- [2] Janssen P M and Hoff E I 2012 Teaching NeuroImages: Subacute intracerebral hemorrhage mimicking brain tumor *Neurology* **79** e183
- [3] Maher K P and Malone J F 1997 Computerized scatter correction in diagnostic radiology *Contemp. Phys.* **38** 131–48
- [4] Gao H *et al* 2010 Scatter correction method for x-ray CT using primary modulation: phantom studies *Med. Phys.* **37** 934–46
- [5] Baer M and Kachelrieß M 2012 Hybrid scatter correction for CT imaging *Phys. Med. Biol.* **57** 6849–67
- [6] Shrimpton P C, Wall B F and Fisher E S 1981 The tissue-equivalence of the Alderson Rando anthropomorphic phantom for x-rays of diagnostic qualities *Phys. Med. Biol.* **26** 133–9
- [7] Sisniega A *et al* 2015 High-fidelity artifact correction for cone-beam CT imaging of the brain *Phys. Med. Biol.* **60** 1415–39
- [8] Chiarot C B *et al* 2005 An innovative phantom for quantitative and qualitative investigation of advanced x-ray imaging technologies *Phys. Med. Biol.* **50** N287–97
- [9] Geraldelli W, Tomal A and Poletti M E 2013 Characterization of tissueequivalent materials through measurements of the linear attenuation coefficient and scattering profiles obtained With Polyenergetic Beams *IEEE Trans. Nucl. Sci.* **60** 566–71
- [10] Kozanetzky J *et al* 1987 X-ray diffraction measurements of some plastic materials and body tissues *Med. Phys.* **14** 526–32
- [11] Kim J I *et al* 2006 Physical phantom of typical Korean male for radiation protection purpose *Radiat. Prot. Dosim.* **118** 131–6
- [12] Akhlaghi P, Hakimabad H M and Motavalli L R 2015 Determination of tissue equivalent materials of a physical 8-year-old phantom for use in computed tomography *Radiat. Phys. Chem.* **112** 169–76
- [13] Ximenes R E *et al* 2015 Development of an anthropomorphic head phantom using dolomite and polymethyl methacrylate for dosimetry in computed tomography *Radiat. Phys. Chem.* **117** 203–8
- [14] Gallas R R *et al* 2015 An anthropomorphic multimodality (CT/MRI) head phantom prototype for end-to-end tests in ion radiotherapy *Z. Med. Phys.* **25** 391–9
- [15] Jones A K, Hintenlang D E and Bolch W E 2003 Tissue-equivalent materials for construction of tomographic dosimetry phantoms in pediatric radiology *Med. Phys.* **30** 2072–81
- [16] Singh Mann K, Kurudirek M and Sidhu G S 2012 Verification of dosimetric materials to be used as tissue-substitutes in radiological diagnosis *Appl. Radiat. Isot.* **70** 681–91
- [17] Poletti M E, Gonçalves O D and Mazzaro I 2004 Measurements of X-ray scatter signatures for some tissue-equivalent materials *Nuclear Instruments and Methods in Physics Research, Section B: Beam Interactions with Materials and Atoms* **213** 595–8
- [18] Berger M J *et al* 1998 XCOM: Photon Cross Sections Database (<http://physics.nist.gov/PhysRefData/Xcom/Text/version.shtml>) (visited on 11/10/2016)
- [19] ICRU 1989 Tissue substitutes in radiation dosimetry and measurement *Tech. Rep.* 44 Bethesda, MD
- [20] Cooper V N *et al* 2000 An edge spread technique for measurement of the scatter-to-primary ratio in mammography *Med. Phys.* **27** 845–53
- [21] Lazos D and Williamson J F 2012 Impact of flat panel-imager veiling glare on scatter-estimation accuracy and image quality of a commercial on-board cone-beam CT imaging system *Med. Phys.* **39** 5639
- [22] Salvat F, Fernandez-Varea J M and Sempau J 2006 Penelope-2006: A code system for monte carlo simulation of electron and photon transport *CEUR Workshop Proceedings* **4** 7
- [23] Badal A and Badano A 2009 Accelerating monte carlo simulations of photon transport in a voxelized geometry using a massively parallel graphics processing unit *Med. Phys.* **36** 4878–80
- [24] Ali M F and Ray S 2013 SAR analysis for handheld mobile phone using DICOM based voxel model *Journal of Microwaves, Optoelectronics and Electromagnetic Applications* **12** 363–75